Anode position influence on discharge modes of a LaB 6 cathode in diode configuration

George-Cristian Potrivitu, Romain Joussot, Stéphane Mazouffre

Anode position influence on discharge modes of a LaB_6 cathode in diode configuration

George-Cristian Potrivitu[a,*], Romain Joussot[a], Stéphane Mazouffre[a]

[a] *CNRS, ICARE, UPR3021, 1C av. Recherche Scientifique, CS 50060, F-45071, Orléans cedex 2, France*

Abstract

Cathodes are electron sources whose operation is based on thermionic emission of electrons. A laboratory model of a 5 A-class cathode was experimentally studied in diode configuration with a disk anode. The core of the cathode is a flat disk lanthanum hexaboride (LaB_6) insert. Electron emission is achieved using a heating element in direct contact with the insert. The paper reports the characterization of the LaB_6 cathode operated at xenon mass flow rates between 0.4 and 1.0 mg s^{-1} with discharge currents ranging from 2 to 12 A. Besides the operating envelope and discharge mode (spot versus plume) differentiation, the influence of anode position on cathode discharge mode was studied. For this last purpose, the cathode was operated at 4 A and 0.6 mg s^{-1} and at 10 A and 0.6 mg s^{-1}, while the cathode-anode gap was increased from 20 mm to 70 mm. Both electrical and plasma parameters were collected and analyzed in order to highlight the main cathode discharge changes when the cathode-anode gap was increased. A particular attention was paid to the identification of the discharge mode and mode transition based on spectral analysis of discharge current waveforms.

Keywords: Electron source, Cathode, Anode, Langmuir probe, Electric propulsion

1. Introduction

A Hall thruster (HT) employes a cathode, as source of electrons, along with an anode in order to ionize the propellant gas. During thruster operation, the cathode provides electrons towards the anode to counterbalance losses and maintain the plasma discharge. A large fraction of electron current is also used for neutralization of the ion flow downstream the thruster outlet. This last fraction of the cathode electron stream typically accounts for 80% of the total cathode electron current [1]. The cathode, along with the magnetic circuit, remain one of the critical components of a Hall thruster, drastically influencing the system performances and lifespan [2].

The core of a cathode is the emitting element, namely the insert, shaped as a flat disk or a hollow cylinder. The insert material can be a refractory metal, such as tungsten, tantalum or molybdenum, or more complex materials, such as lanthanum hexaboride (LaB_6), barium oxide impregnated into a porous tungsten matrix (BaO-W) or calcium aluminate, known as electride (C12A7) [3, 4]. In particular, lanthanum hexaboride is considered as a reliable material for a cathode insert, allowing for simplified handling and start-up procedures [5], longer simulated lifetimes [5] due to its lower evaporation rate, robustness to impurity poisoning and water vapors [3, 6]. However, a LaB_6 insert must be operated at elevated temperatures due to its relatively high work function [3]. This requires heater devices capable of delivering high temperatures which may lead to greater risk of failures [7]. This last aspect is of great importance when developing high power Hall thrusters and it is therefore under consideration by several research teams [7, 8, 9].

During the development and characterization phases, cathodes are usually tested in diode configuration with an external anode. Different anode geometries, as well as different cathode to anode distances, may lead to a broad set of results, making difficult the comparison between various cath-

*Corresponding author
Email address:
george-cristian.potrivitu@cnrs-orleans.fr
(George-Cristian Potrivitu)

odes discharge characteristics. This contribution presents the results obtained during the characterization phase of a 5 A-class LaB_6 cathode, underlying the influence of anode position on cathode discharge mode. The cathode is based on a flat disk LaB_6 insert, emitting electrons via thermionic emission after being sufficiently heated by a tungsten wire heater. Few studies are available on discharge characterization of cathodes with disk-shaped emitters [10, 11], although this design is used by several research teams [12, 13, 14, 15]. Moreover, the influence of anode position on cathode discharge mode is poorly documented in the literature [16, 17, 18].

Three aspects regarding the discharge of the laboratory model 5 A-class LaB_6 cathode are discussed. Firstly, the cathode discharge envelope (*i.e.*, the discharge electrical parameters) is presented, with the cathode operated in diode configuration with an external stainless steel disk anode placed 20 mm downstream the cathode orifice. Discharge modes are presented, based on the discharge current waveforms, distinguishing the two main discharge modes [19, 20]: the spot mode and the plume mode. Secondly, the cathode-anode gap was increased from 20 mm to 70 mm in order to observe the influence on cathode discharge mode. During experiments the cathode was operated at 4 A and 0.6 mg s^{-1}, starting in the spot mode and at 10 A and 0.6 mg s^{-1}, with an initial discharge in the plume mode. Lastly, the influence of anode position on plasma properties, *i.e.* plasma potential, density and electron temperature, was investigated by single Langmuir probe measurements in the cathode plume.

2. Experimental setup

2.1. The NExET test bench

The cathode was tested in diode configuration in the NExET test bench, see Fig. 1 [11]. The chamber, made of stainless steel, has a diameter of 0.8 m and a total length of 1.8 m. In order to attain pressures down to 10^{-6} mbar-N_2, the vacuum chamber is equipped with a large dry pump and a 350 L s^{-1} turbomolecular pump to evacuate light gases. Moreover, a cryogenic pump with a pumping speed of 8000 L s^{-1} and typical surface temperature of 25-35 K is employed, in conjunction with the turbomolecular pump, to absorb gases such as Xe and Kr [11]. The interior of the chamber is accessed trough a wide door located at the front of the chamber. A fraction of the ion beam energy is absorbed by a large screen covered with graphite and placed at the back of the chamber. In this way the thermal load on the cryogenic surface is limited.

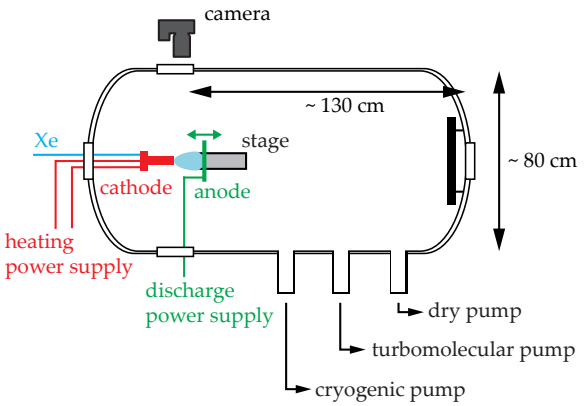

Figure 1: Schematic of the NExET vacuum chamber with the cathode-anode system setup.

A background pressure inside NExET of 2×10^{-5} mbar-Xe is achieved with 1 mg s^{-1} xenon gas flow rate and 250 W input power [11]. A quick calculation reveals that in this pressure condition the heavy particle momentum exchange mean free path is of the order of the vacuum chamber length, therefore the residual gas has a negligible impact on the results. Several observation windows provide view access to the interior of the chamber which is also equipped with several power, gas and diagnostic feedthroughs.

2.2. Cathode setup configuration

The cathode design used in this study is based on a laboratory model employed usually with the SPT-100-ML [21], a 1.5 kW Hall thruster derived from the Russian SPT-100 [22]. The usual cathode design used in our works is based on the heating of a flat disk LaB_6 insert (Fig. 2) at temperatures high enough to allow thermionic emission of electrons. The emitter has a diameter of 8 mm and a thickness of 2 mm, being made of sintered (*i.e.*, polycrystalline) LaB_6. To keep the emitter in place, a molybdenum holder is used. The holder has an opening of 6 mm in diameter, imposing a total emission area of 28.27 mm^2. In order to heat up the emissive element, a tungsten spring is used, connected to the heating circuit. The LaB_6 insert, the molybdenum holder, and the heating filament are wrapped in molybdenum foil, kept in place by several molybdenum hoops. This provides insulation

in order to minimize radiative losses during emitter heating [11]. These three elements form the internal body of the cathode. The external body has a cylindrical shape with a diameter of 25 mm and a total length of 95 mm. The external body allows the use of a removable orifice plate. In this study the results are for a cathode with a 3 mm-diameter orifice with an aspect ratio (*i.e.*, ratio between the orifice length and its diameter) of 0.33. The orifice plate is fixed against the external body by the means of four threatened molybdenum rods and four tantalum nuts, while a 0.1 mm thick pyrolytic graphite sleeve was used between parts to provide good sealing. Xenon (N48 grade, 99.998% purity) injection is provided via a gas feed connection attached to the external body. The internal parts and the external body are fixed to a ceramic plinth by the means of a screw. In order to facilitate the cathode discharge, an external igniter is used, positively biased with respect to the cathode body (*i.e.*, internal body). The igniter is placed in the vicinity of the cathode orifice and at a distance of about 4 mm. The external body of the cathode is kept electrically floating during the cathode operation. Moreover, no keeper electrode was required in order to properly operate the cathode within the current range presented in this work. Furthermore, the external igniter is not necessary, since the external body can act as an igniter, simplifying the cathode design. It was found that this cathode design allows self-heating stable operation at a discharge current of 5 A and a nominal mass flow rate of 0.4 mg s^{-1} of Xe [23].

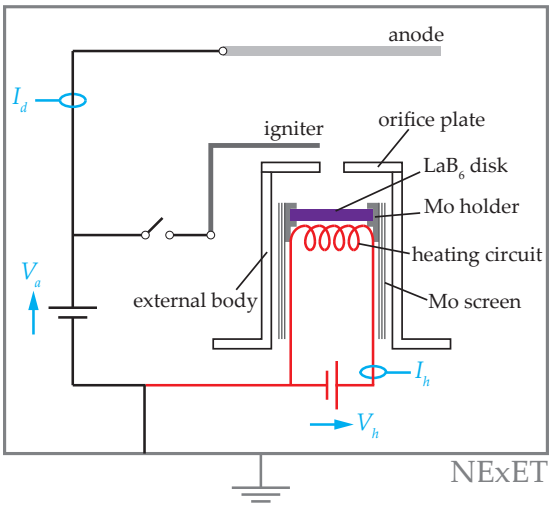

Figure 2: Schematic of the electrical setup for the cathode in diode configuration with the disk anode.

During the tests, the cathode was operated in diode configuration together with an external anode. The latter was a non-magnetic stainless steel disk with an outer diameter of 110 mm, providing a surface in front of the cathode of around 95 cm^2. By making the anode positively biased with respect to the cathode internal body, the electrons extracted from the emitter surface are accelerated towards the anode. Fig. 2 depicts the schematic of the electrical setup.

The distance d_{gap} between the cathode exit plane and the anode can be modified from 20 mm to 70 mm, since the anode is placed on a translation stage. For Langmuir probe measurements, two Zaber A-series Vacuum Motion Positioners were used in xy configuration and controlled by two Zaber X-MCB2 stepper motor controllers.

2.3. Electrical measurements

The cathode heating power was delivered by a Midec power supply (SK 40-25, 40 V, 25 A). The main discharge power (*i.e.*, cathode-anode discharge) was assured by an Elektro-Automatik power supply (EA-PSI 9200-70, 200 V, 70 A, 5 kW). The igniter was connected to this last power supply via a switch. The cathode base was grounded, while the external body of the cathode was floating throughout all experiments.

For the cathode discharge envelope measurements, the anode voltage was measured using a Tektronix voltage probe (P6139A, 500 MHz, 8.0 pF). The discharge current (*i.e.*, the anode current) was measured using a Tektronix current probe (TCP202, dc to 50 MHz bandwidth). Both probes were connected to a Tektronix digital oscilloscope (TDS5104, 1 GHz, 5 GS s^{-1}). The electrical waveforms were recorded at sampling frequency of 500 kHz and a cut-off frequency of 250 kHz, enough to catch the usual oscillating phenomena that the discharge current and voltage may exhibit in the plume of a cathode [11].

For the measurements regarding the influence of anode position on cathode discharge mode, the anode voltage was measured using a LeCroy voltage probe (PP018, 500 MHz, 10:1, 10.0 pF). The discharge current was measured using a LeCroy current probe (AP015, dc to 50 MHz bandwidth). The probes were connected to a LeCroy high definition digital oscilloscope (HD060104, 1 GHz, 2.5 GS s^{-1}) to monitor and record the electrical signals at a sampling rate of 1 MHz and a cut-off frequency of 500 kHz.

The Langmuir probe measurements were conducted along the cathode axis and data was recorded using an Impedans ALP system.

3. Operating envelope

The external body of the cathode was thicker than the one of the cathode previously tested by our team [11]. For that reason, for the discharge to occur, the heating current I_h was raised at 16 A, while the heating circuit potential V_h stabilized around the value of 14.5 V. Therefore, a total heating power of about 230 W was delivered to the LaB_6 insert in order to initiate the discharge. The starting sequence, as well as all tests, were conducted with the main discharge power supply working in a current-regulated configuration, namely the discharge current I_d was kept fixed, while the discharge voltage (*i.e.*, the anode voltage) V_a was adapted by the supply in order to match the circuit's charge. The cathode was started at 2 A and voltage limited at 200 V, while a flux of 0.6 mg s^{-1} of xenon was passed through it. The 200 V were firstly applied, in the starting sequence, to the external igniter in order to ease the cathode start-up. After the starting sequence finished, the cathode was run for 900 s before the heating circuit was turned off, leaving the cathode in a self-heating operation. The following results were obtained for the cathode in this particular operation mode. The anode was placed at a distance of 20 mm from the cathode exit plane.

In order to construct the discharge envelope, the cathode was operated at discharge currents between 2 A and 12 A and at four mass flow rates of xenon (0.4 mg s^{-1}, 0.6 mg s^{-1}, 0.8 mg s^{-1}, and 1 mg s^{-1}). The background pressure varied between 3×10^{-5} mbar-Xe and 6×10^{-5} mbar-Xe, respectively. Between each change in xenon mass flow rate or in discharge current, the cathode was run for 600 s before the oscilloscope traces were recorded, assuring a steady state discharge. Fig. 3a depicts the anode potential V_a as a function of the discharge current I_d for the four xenon mass flow rates. In order to distinguish between spot mode and plume mode operation, the discharge current recorded waveforms were used. The standard deviation of the discharge current $I_{d,std}$ was calculated using the classical unbiased estimator. Furthermore, the ratio of $I_{d,std}$ to I_d was computed for each discharge point. The results are presented in Fig. 3*b*, where the dashed red line at $I_{d,std}/I_d = 9\%$ is the threshold for spot-plume transition, independent of the mass flow rate [24].

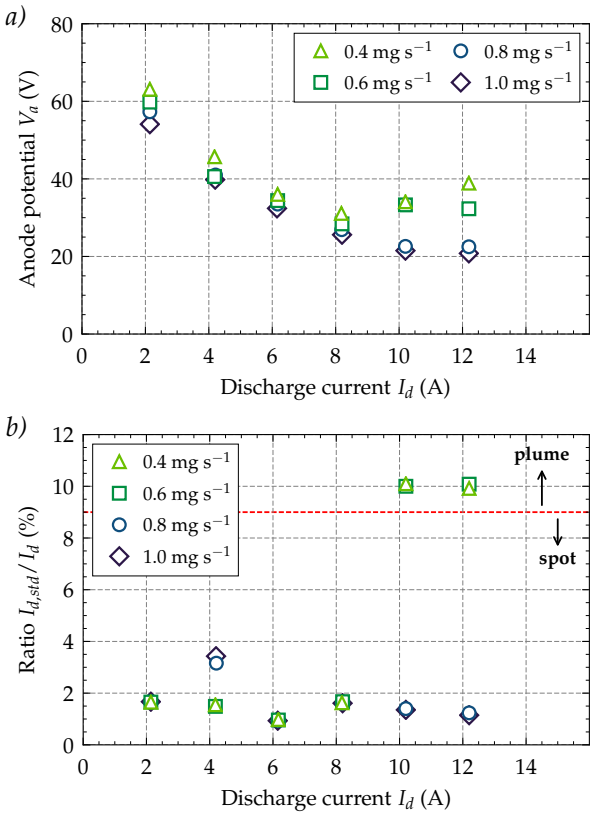

Figure 3: Electrical parameters of the LaB_6 cathode in diode configuration: *a)* anode potential V_a and *b)* ratio of the standard deviation of I_d to the average value of I_d versus the discharge current for different mass flow rates of Xe. The cathode-anode gap is 20 mm. The dashed red line corresponds to $I_{d,std}/I_d = 9\%$ [24].

Within the discharge current range, two main tendencies prevails. Firstly, one may observe that the anode potential decreases with the increase in discharge current. Secondly, at a given discharge current, the higher the mass flow rate, the lower the anode potential, as expected [25]. If the second trend in the cathode discharge envelope is comprehensible, the first behavior is rather counter intuitive, since one may expect higher anode potentials at higher discharge currents, when plume mode operation is observed [11, 16, 26, 27]. However, this first behavior was already observed by other research teams [17, 28]. At low mass flow rates (0.4 mg s^{-1} and 0.6 mg s^{-1}) the cathode operates in spot mode up to 8 A of discharge current, with a decrease in the anode potential of about 30 V

over the discharge current interval. Fluctuations of the electrical parameters of the discharge are very low, under 2% of the average value. When the discharge current is further increased to 10 A and then to 12 A, the anode potential slightly increases with 5 V and 10 V, respectively, with respect to the value recorded at 8 A. Moreover, the discharge becomes noisier, and the cathode mode transitions to plume mode with a ratio $I_{d,std}/I_d$ of about 10%. For higher mass flow rates (0.8 mg s^{-1} and 1 mg s^{-1}) the cathode operates in spot mode over the entire range of discharge currents. As in the case of low mass flow rates, the increase in the discharge current induces a decrease in the anode potential of about 30 V over the discharge current interval. Fluctuations of the electrical parameters of the discharge are very low, under 2% of the average value, for all the discharge current values except for $I_d = 4$ A, when the ratio $I_{d,std}/I_d$ reaches 3.5%.

Analyzing the power spectral densities of the discharge current (not shown here), it is observed that the plasma plumes downstream the cathode orifice is characterized by frequencies in the range 60 to 80 kHz, in agreement with previous results [11]. The frequency of the fundamental peak seems to increase with the discharge current and decrease when the mass flow rate is increased. Similar behaviors were previously reported in literature [29, 30, 31]. In general, the spot modes have less energetic spectra, since the level of fluctuations is lower than in the case of the plume modes. However, for the spot modes at 10 A and 12 A, the spectra exhibit narrow peaks at frequencies between 80 and 90 kHz, decreasing with the increase in the discharge current. This confirms that the transitions between the two modes occur in a continuous manner [11, 30].

4. Anode position influence on discharge modes

After the discharge envelope characterization, the cathode-anode system was employed in a study aimed at the understanding of the influence of anode position on cathode discharge mode. Several studies exist on cathode position influence on Hall thruster discharge characteristics [32, 33]. However, the influence of anode position on cathode discharge mode in diode configuration (without the presence of a thruster magnetic field), is less documented in the literature. A reliable source on the subject remains the study conducted by Csiky [16] with a hollow cathode. According to Csiky, the cathode tends to change from spot mode to plume mode operation as the cathode-anode gap increases, and depending on the mass flow rate there may exist an interval of cathode-anode gap values for which the cathode operates either in spot or plume mode, depending on the electron emission thresholds [16].

Since our cathode design is based on a flat disk LaB_6 emitter and it shows a counter intuitive behavior, it was interesting to investigate the influence of anode position on cathode discharge mode. Therefore, this work presents the first results for a flat disk LaB_6 cathode. For this purpose, the cathode was operated at a constant xenon mass flow rate of 0.6 mg s^{-1} and, once at a time, at a discharge current of 4 A, corresponding to a spot mode discharge, and 10 A, corresponding to a plume mode discharge, respectively. The first cathode-anode gap was set at 20 mm and then the gap was increased up to 70 mm. Between each change in the cathode-anode gap the cathode was operated for 900 s before the oscilloscope traces were recorded.

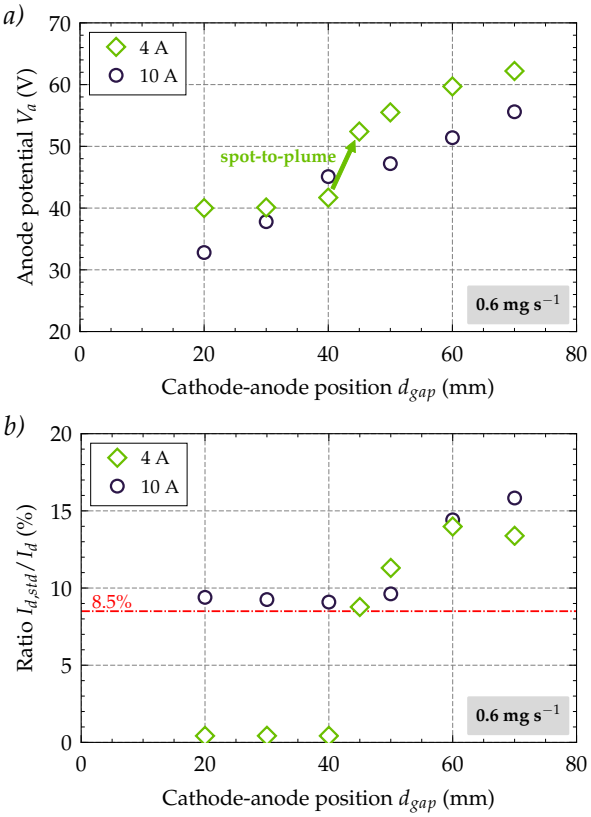

Figure 4: Electrical parameters of the LaB_6 cathode in diode configuration at a Xe mass flow rate of 0.6 mg s^{-1}: *a)* anode potential V_a and *b)* ratio of the standard deviation of I_d to the average value of I_d versus the cathode-anode gap.

Fig. 4*a* depicts the anode potential as a function of the cathode-anode gap d_{gap}. When the cathode is initially in a spot mode (4 A) and the cathode-anode gap is increased, the anode voltage remains almost constant till the gap reaches 40 mm and the cathode displays a spot mode operation. At a gap value of 45 mm the discharge mode transitions to a plume mode with a higher discharge voltage, a jump of almost 10 V. As the cathode-anode gap is further increased, the anode potential increases as well and the cathode exhibits plume mode operation. Several tests were conducted by increasing the cathode-anode gap or decreasing it back to 20 mm, and the transition point was observed to be conserved in the vicinity of the gap value of 45 mm, with some hysteresis. Mode transition can be easily visualized if the ratio $I_{d,std}/I_d$ is plotted against the cathode-anode gap, as depicted in Fig. 4*b*. Up to the gap value of 40 mm, the fluctuations of the electrical parameters of the discharge are very low, under 2% of the average value. At a gap value of 45 mm the ratio $I_{d,std}/I_d$ reaches about 9% and further increases to about 14% at 60 mm of gap. On the other hand, when the initial discharge mode is a plume mode (10 A), the anode potential increases almost linearly with the cathode-anode gap, with an increment of almost 20 V over the range of gap values. The cathode exhibits a relatively quiescent plume mode operation with the $I_{d,std}/I_d$ about 9% up to the value of 50 mm for the cathode-anode gap. Further increase in the gap value induces a noisier plume mode with fluctuations of the electrical parameters of the discharge reaching over 15% of the average value at a gap value of 70 mm. Hereinafter, a detailed discussion on the physics of the two aforementioned cases ensues.

4.1. Initial spot mode case: 4 A *at* 0.6 mg s^{-1}

Visually, the cathode plume morphology shows few typical characteristics related to the operation mode. Fig. 5*b*-*h* depicts photographs of the cathode discharge plume for the initial spot mode case (4 A and 0.6 mg s^{-1}). Up to a cathode-anode gap value of 40 mm, the cathode exhibited a spot mode operation. Visually, the cathode plume presents a spot-like bright structure [25] close to the cathode orifice, displaying a blue coloring due to the high density of xenon ions (Fig. 5*b*-*d*). The fast electrons produced by the cathode in this operating mode induce ionization and excitation of the neutral atoms near the cathode exit plane, while the rest of the cathode-anode space remains dark (less luminous) [16]. However, despite the classical morphology of the spot mode discharge aforementioned, the tested cathode shows a particular spot mode plume morphology: instead of a sole, bright, spot-like structure next to the cathode orifice, a more brightly plume is observed, diffusely attached to the anode.

When the cathode-anode gap is further increased, the cathode discharge transitions to plume mode operation. At the gap value of 45 mm the transition is sudden and visually observed, as well as noticed in the abrupt rise in the discharge electrical parameters fluctuations. Visually, the plume of the cathode is less focused with a large divergence angle, brighter and with violet coloring that characterize the high content of excited xenon neutrals instead of ions (Fig. 5*e*-*h*). The ionization and excitation events occur in the far field plume too, due to fast electrons escaping the sheath formed in front of the cathode orifice [16]. Moreover, during most of the plume modes the cathode plume is distinctively composed of a bright region next to the cathode tip and a less bright, more diffuse region attached to the anode. The two regions are separated by a well-defined dark space [29, 30, 34, 35]. The drop in plume's luminosity in this region is due to a low electron temperature, which, in turn, induces a decrease in the xenon atoms excitation rate [34]. This dark-space has the tendency to change its width and location with respect to the cathode exit plane as the cathode-anode gap is changed.

Besides the interpretations based on the plume morphology, the cathode operation mode transition can be identified based on the discharge electrical parameters variation. Time series of the discharge current are valuable indicators of the cathode discharge mode, directly related to plasma development and evolution. Fig. 6 presents the temporal waveforms of the discharge current for different cathode-anode gap values and for the initial spot mode case. For a cathode-anode gap of 30 mm the discharge current exhibits a very low level of fluctuations, indicating a spot mode operation. As the cathode-anode gap is increased, a growing level of fluctuations appears in the discharge current waveforms. Since the xenon mass flow rate remains constant throughout the process, the increase in the discharge current fluctuations induced by the increase in the cathode-anode gap, is similar to the one induced by the increase in the discharge current, tendency thoroughly discussed in literature [25, 30] and explained by the axial profile of the neutral density in the cathode plume.

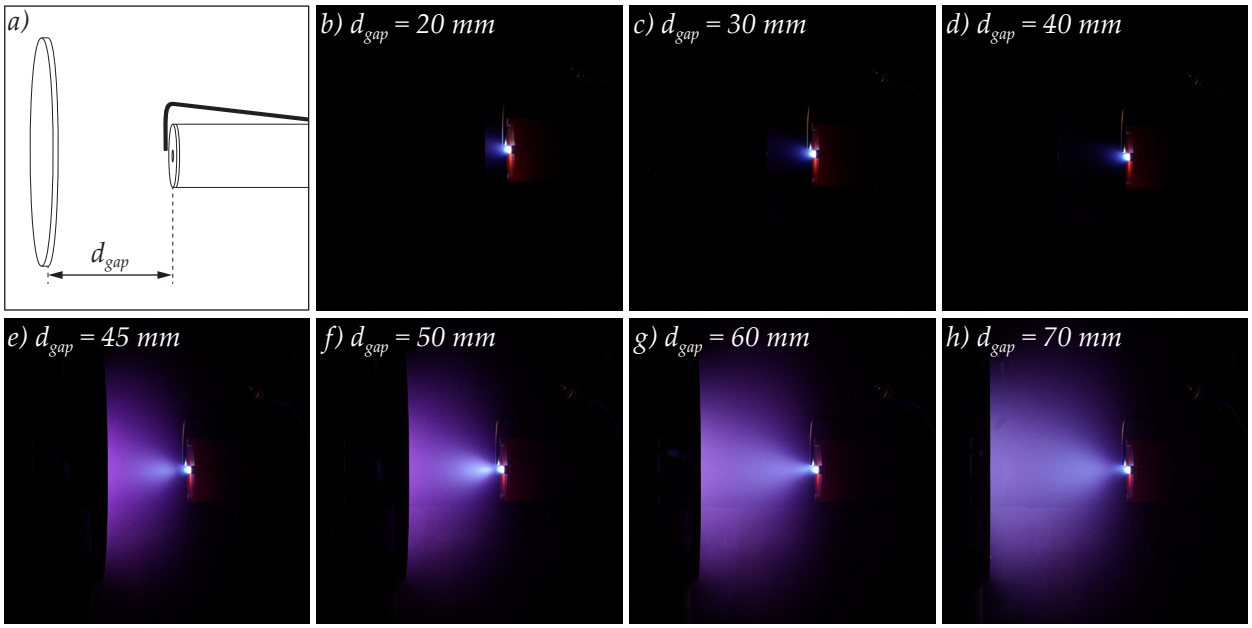

Figure 5: *a)* Schematic of the cathode-anode setup with the gap distance d_{gap} between the cathode body and the anode and *b-h)* photographs of the cathode discharge plume for cathode-anode gap values between 20 mm and 70 mm. The discharge current is 4 A and the Xe mass flow rate is 0.6 mg s^{-1}. All photographs have the same exposure time.

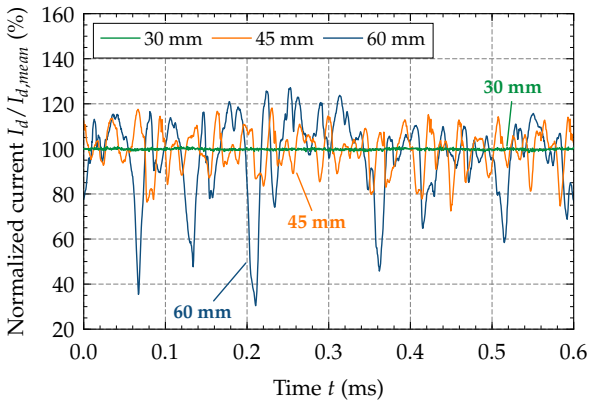

Figure 6: Time series of the normalized discharge current ($I_d/I_{d,mean}$) for different cathode–anode gaps. The discharge current is 4 A and the Xe mass flow rate is 0.6 mg s^{-1}.

In the case of the spot mode operation, the discharge plasma has high enough densities to sustain a passive electron current towards the anode [36, 37]. In the cathode plume, low electron temperatures are reached, since the collisional regime is strong and small electron repelling sheaths are formed near the anode [36, 37]. Those sheaths form only when the passive plasma currents collected by the anode are sufficient or over the net current needed for proper functioning [38]. On the other hand, when the passive current to the anode is not sufficient to sustain the desired discharge current, electron attracting sheaths form and increase the collected current towards the anode. The low plasma density fails to produce the necessary current and the anode potential starts to increase due to the formation of the electron attracting sheaths [38]. This is the case of a plume mode operation.

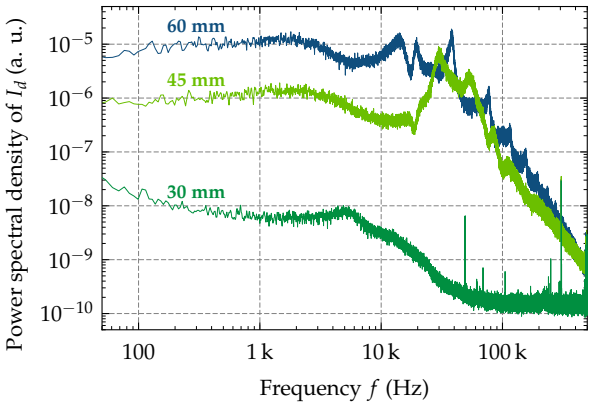

Figure 7: Power spectral density of the discharge current for different cathode-anode gaps. The discharge current is 4 A and the Xe mass flow rate is 0.6 mg s^{-1}.

Based on the discharge current waveforms, the power spectral density and histograms can be computed, providing more insights regarding the influence of anode position on cathode discharge mode. Power spectral density (PSD) of the discharge current is estimated and plotted using Welch method. Fig. 7 presents the power spectral densities for three cathode-anode gap values. For the spot mode observed at a gap value of 30 mm, the power spectrum is less energetic, in accordance with the low level of discharge current fluctuations recorded (under 2% of the average value). No fundamental frequency peak is recorded, for frequencies higher than 10 kHz (the narrow peaks in the spectra are most probably measurement artifacts). As the cathode-anode gap is increased, the quiescent spectra, typical for spot modes, becomes more energetic. In fact, for the plume modes the average energy of the PSDs is few orders of magnitude greater than the one found for the spot modes. Moreover, both in fundamental frequency and its harmonics, the spectra displays broader peaks. The frequency of the fundamental is detected between 40 kHz and 60 kHz, decreasing with the increase of the cathode-anode gap value. This is a typical range of frequencies depicting the emergence of ionization-like instabilities, in the cathode plume [31, 39, 40, 41]. Moreover, the average energy of the spectra increases with the cathode-anode gap.

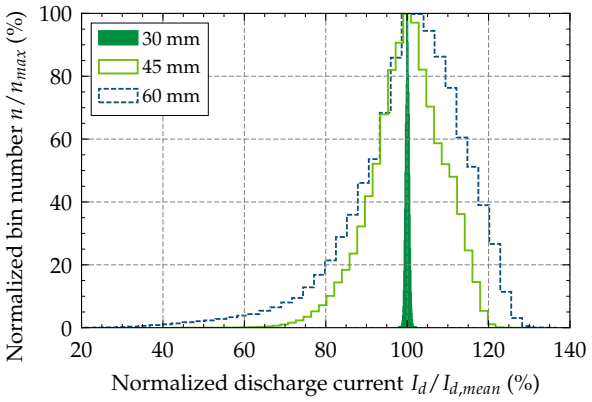

Figure 8: Histogram of the discharge current for different cathode-anode gaps. Bin numbers n are normalized with the maximum bin number n_{max}. The bins (class intervals) are expressed in terms of normalized discharge current $I_d/I_{d,mean}$. The discharge current is 4 A and the Xe mass flow rate is 0.6 mg s^{-1}.

Fig. 8 presents the discharge current histograms for several cathode-anode gaps. The center of the histogram corresponds to a ratio $I_d/I_{d,mean} = 100\%$, lower values of this ratio correspond to the negative part of the histogram (*i.e.*, discharge current lower than the mean value), while the positive part corresponds to value higher than 100% (*i.e.*, discharge current higher than the mean value). For the initial spot mode case, the discharge current histograms are unimodal for all cathode-anode gap values. One can easily observe that for the cathode-anode gap of 30 mm the histogram is narrow, compared with the ones obtained for higher cathode-anode gap values, suggesting a low fluctuation of the discharge current around its nominal value, and therefore the prevalence of a spot mode operation. The increase in the cathode-anode gap broaden the discharge current histograms, in accordance with the higher level of fluctuations in this parameter. Furthermore, one can observe that the negative skewness (*i.e.*, negative part tail) of the discharge current histograms surpassed the positive skewness as the cathode-anode gap value increases. Moreover, by observing the the discharge current waveforms (Fig. 6), the negative part kurtosis of the waveform is higher than the one characterizing the positive part, the difference between the two increasing with the cathode-anode gap. This is translated into a much rapid change in the waveform slope in its negative part than in the positive one as well as higher deviation from the mean value of the discharge current in the negative part than in the positive one, both phenomena being induced by the increase in the cathode-anode gap translated into noisier plume mode operation.

4.2. Initial plume mode case: 10 A *at* 0.6 mg s^{-1}

We have already seen that when the cathode-anode gap is increased, an initial spot mode cathode operation can transition to a plume mode, with a series of implications in the electrical parameters, and in particular the discharge current. It is worth investigating anode position influence on cathode discharge when initially (d_{gap}=20 mm) the cathode operates in a plume mode.

From visual inspection of the cathode plume morphology (Fig. 9), one can notice bright plume structures, diffusely attached to the anode. Furthermore, most of the plumes displays a complex structure composed of two regions: a bright region next to the cathode orifice and a more diffuse region attached to the anode. Between the two regions, a dark space is clearly distinguished in the photographs. The coloring of the plume shows vio-

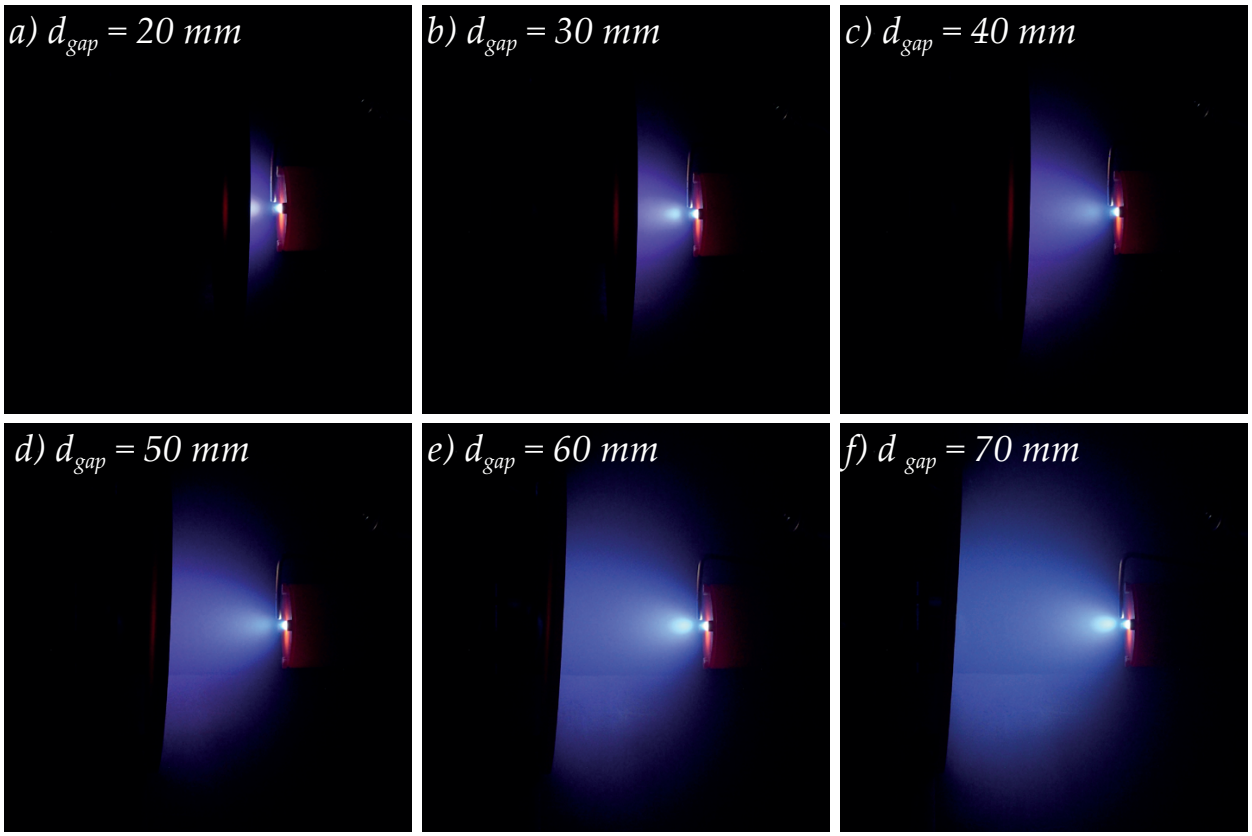

Figure 9: *a-f)* Photographs of the cathode discharge plume for cathode-anode gap values between 20 mm and 70 mm. The discharge current is 10 A and the Xe mass flow rate is 0.6 mg s^{-1}. All photographs have the same exposure time.

let shades (Fig. 9*a-c*) which are replaced by more blue tones as the cathode-anode gap is increased (Fig. 9*d-f*). This last aspect may suggest a better level of ionization as the cathode-anode gap is increased. At the gap value of 20 mm, a bright region forms in the anode vicinity, suggesting high rates of ionization. It is observed for several gap values (30 mm, 60 mm and 70 mm), that besides the luminous region next to the cathode tip, a second bright region appears right after the dark space, in the cathode far-field plume, suggesting the presence of a second zone with high rates of ionization. The second zones with high ionization rates may be induced by energetic electrons escaping the sheath formed in front of the cathode during plume operation [16], while potential structure in the far-field plume can induce or maintain high energy electrons. Moreover, due to the high power levels of the discharge (more than 320 W), a high electric field is sustained in the anode sheath, and therefore energetic electrons are produced. Anode material evaporation and sputtering can lead to the ionization of the anode metallic atoms, creating the bright region observed right next to the anode for d_{gap}=20 mm.

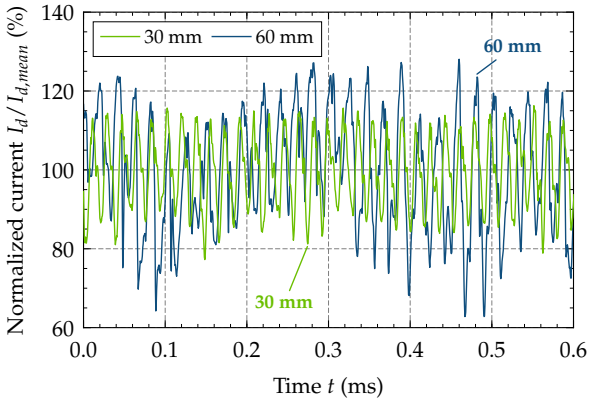

Figure 10: Time series of the normalized discharge current ($I_d/I_{d,mean}$) for different cathode-anode gaps. The discharge current is 10 A and the Xe mass flow rate is 0.6 mg s^{-1}.

Time series of the discharge current for different

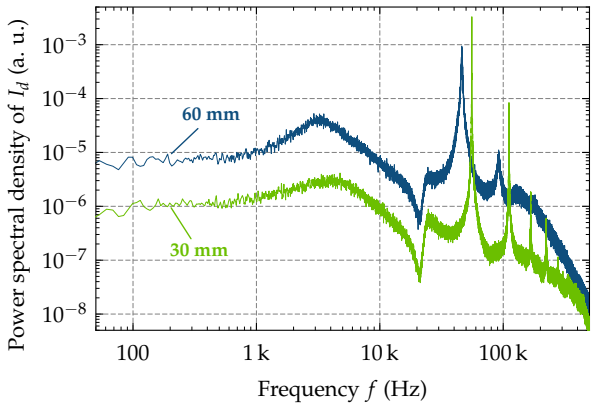

Figure 11: Power spectral density of the discharge current for different cathode-anode gaps. The discharge current is 10 A and the Xe mass flow rate is 0.6 mg s^{-1}.

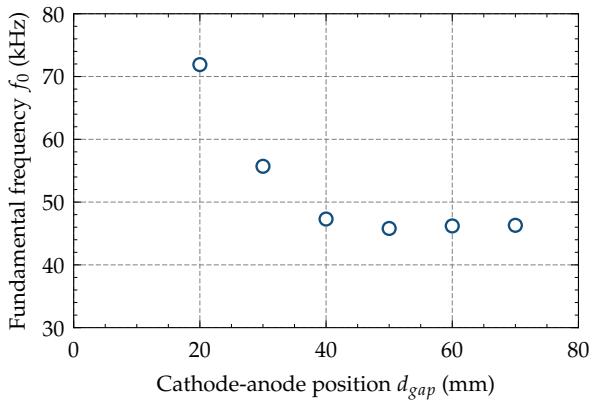

Figure 12: Fundamental frequency f_0 of the discharge current oscillations according to the cathode-anode gap. The discharge current is 10 A and the Xe mass flow rate is 0.6 mg s^{-1}.

cathode-anode gap values are presented in Fig. 10. As expected, high levels of discharge current fluctuations are observed for all the cathode-anode gap values, suggesting the plume mode operation of the cathode. As the gap value increases, the level of fluctuations in the discharge current increases as well, which translates into higher energy of the power density spectra. Fig. 11 shows two spectra for the gap values of 30 mm and 60 mm. One can observe the distinctive fundamental frequency peak and its associated harmonics. Moreover, as the gap increases, the fundamental peak became broader and the spectrum more energetic, features observed when usually an increase in the discharge current occurs [11]. It is also observed that the fundamental frequency of the discharge current power

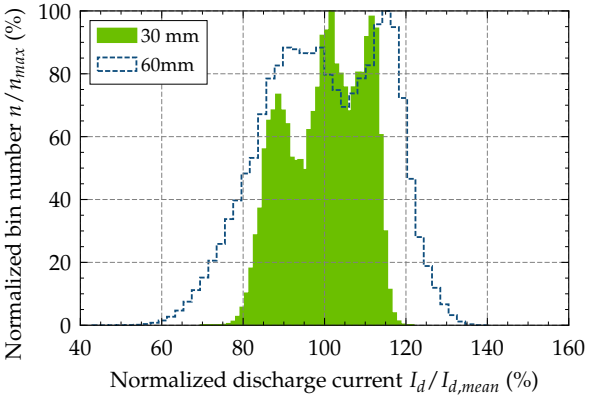

Figure 13: Histogram of the discharge current for different cathode-anode gaps. Bin numbers n are normalized with the maximum bin number n_{max}. The bins (class intervals) are expressed in terms of normalized discharge current $I_d/I_{d,mean}$. The discharge current is 10 A and the Xe mass flow rate is 0.6 mg s^{-1}.

spectra ranges between 45 kHz and 72 kHz over the cathode-anode gap values, as presented in Fig. 12. Once again, this range of frequencies suggests the presence of ionization-like instabilities in the cathode plume [31, 39, 40, 41]. Another important feature suggested by Fig. 12 is that the fundamental frequency decreases as the cathode-anode gap is increased. This particular tendency is observed when the mass flow rate or the discharge current are decreased, since the ionization fraction is lower in this case [30]. Therefore, it can be concluded that the increase in the cathode-anode gap has a coupled effect on the cathode discharge current spectra: the estimated power spectra energy is increased, as in the case of an increase in the discharge current, and the fundamental frequency is decreased, as in the case of an increase in the mass flow rate. However, there is contradiction, since it is well known that an increase in the discharge current induces an increase in the fundamental frequency as well [11, 29, 30, 31]. Therefore, within the coupled phenomena, the weight of the mass flow rate increase-like behavior prevails over the current increase-like tendency.

Histograms of the discharge current for different cathode-anode gap values are presented in Fig. 13. One can firstly observe that in this case the histograms depict different morphologies than in the initial spot case. Multimode discharge current histograms were recorded for all cathode-anode gap values, implying the existence of superimposed dis-

charge current fluctuations. Oscillations in the order of tens of kHz are superimposed to low frequency oscillations in the order of few kHz. The histograms tend to become broader as the gap value is increased, suggesting higher discharge current fluctuations and more energetic power density spectra. There is no particular skewness and relatively equal kurtosis is observed for the negative and positive parts of the histograms.

5. Anode position influence on plasma properties

A cylindrical single Langmuir probe was made using 0.1 mm-diameter tungsten wire protruding 1.5 mm from a single-bore alumina tube. In order to position the probe at the desired location in the cathode plume, two motion stages were used in xy configuration. During measurements, the probe's tip was perpendicular to the discharge axis.

Probe voltage-current traces, first and second current derivatives were delivered by an Impedans APL System and further processed in order to extract plasma parameters, such as plasma density n_e, electron temperature T_e and plasma potential V_p. Druyvesteyn method [42] was used to compute the electron energy distribution functions (EEDF), based on probe's electron current second derivative. The electron current was found by subtracting the ion current part from the probe's collected current and by taking only the part between floating potential and plasma potential [43, 44]. Plasma potential was found as the probe's current first derivative maximum. Plasma number density and electron temperature were then computed from moments to the EEDF.

In the case of EEDF method, determination of error bars is rather a complex task that prevents a direct quantification of their magnitudes. When all the constitutive parameters that enter into the EEDF computation are known to a high degree of accuracy, Herman and Gallimore [45] predict an error or $\pm 8\%$ in the determination of the EEDF using the Druyvesteyn method. The main uncertainty factor in computing the EEDF remains the plasma potential magnitude. If the first derivative of the probe collected current is used for plasma potential, the accuracy in its identification is approximated to $\pm 10\%$ [46].

Probe measurements were conducted with the cathode operating at a discharge current of 4 A and a xenon mass flow rate of 0.6 mg s^{-1}, while the background pressure under these conditions was 3.6×10^{-5} mbar-Xe. Fig. 14 illustrates the single Langmuir probe results obtained on-axis 10 mm downstream the cathode orifice, when the cathode-anode gap was increased. One can see, in Fig. 14a, that as the cathode-anode gap value remains inferior to 40 mm, the discharge potential and the plasma potential are almost equal, while the cathode operates in a spot mode with less than 2% of discharge current fluctuations with respect to the nominal value. At the gap value of 45 mm, the anode potential overpasses rapidly the plasma potential and the discharge becomes more unstable, with 9% of the average value in discharge current fluctuations. As the gap is further increased, the discharge potential increases with the cathode displaying a plume mode operation.

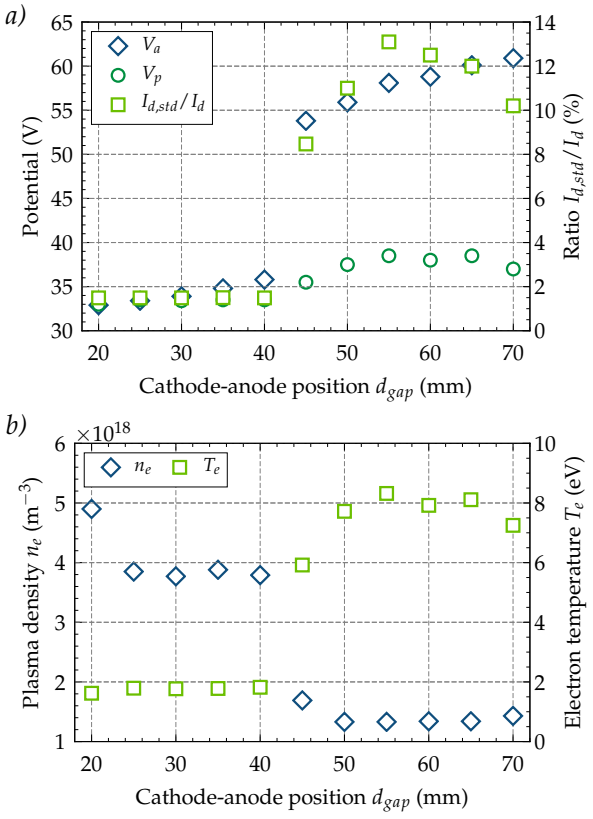

Figure 14: *a)* Anode potential V_a, plasma potential V_p 10 mm downstream the cathode exit plane and ratio $I_{d,std}/I_d$ against the cathode-anode gap; *b)* Plasma number density n_e and electron temperature T_e against the cathode-anode gap at 10 mm downstream the cathode exit plane. The discharge current is 4 A and the Xe mass flow rate is 0.6 mg s^{-1}.

It was interesting to observe the variation of

plasma density and electron temperature at the probed position when the cathode-anode gap was changed. The results are presented in Fig. 14*b*. One can observe that when the cathode-anode gap is around 45 mm the mode transition occurs. For gap values inferior to 45 mm, the electron temperature remains constant around the value of 1.5 eV and after the gap value of 45 mm it increases rapidly up to 8 eV. Plasma number density has an opposite variation. A drop in this plasma parameter of almost three times can be observed over the cathode-anode gap increase.

The increase in the cathode-anode distance induces a higher discharge resistive path, which may induce a constricted attachment of the plume to the anode, due to the formation of an electron attracting sheath at the anode surface. This occurs due to a rapid increase in the thermal electron flux, induced in turn by a discharge power increase.

6. Conclusion

A version of a laboratory model 5 A-class cathode was operated in diode configuration with a disk anode. This cathode model, based on a flat disk LaB_6 emitter, is used together with Hall thrusters as electron source for gas ionization a thruster beam neutralization. When characterizing cathodes as electron sources for solar electric propulsion purposes, an external anode is typically used, placed at a certain distance from cathode exit plane.

This contribution focuses on the investigation of anode position influence on cathode discharge mode. Firstly, we report on the characterization of the cathode discharge, *i.e.* the cathode operating envelope. For this purpose, the discharge current ranged from 2 A to 12 A, while the xenon mass flow rate was varied from $0.4\,\mathrm{mg\,s^{-1}}$ to $1\,\mathrm{mg\,s^{-1}}$. A map of the cathode discharge operating modes was computed, revealing a $1/I_d$ characteristic fall of the anode potential. The cathode displayed spot mode operation over the entire discharge current range and plume mode operation was also noticed for higher discharge currents and low mass flow rates.

Secondly, the cathode-anode gap was modified, with the anode placed on a motion stage. When the cathode operated initially in spot mode (4 A), the increase in the cathode-anode gap induced a sudden change in the discharge mode, from spot to plume, around the gap value of 45 mm and the cathode operated in plume mode for higher gap values. On the other hand, when the initial operation was in plume mode (10 A), the cathode maintained the discharge mode, but with a series of change in plume morphology as well as in the electrical parameters, to note just the most important, an increase in the anode potential and a decrease in the fundamental frequency of the discharge current power density spectra. Evolution of cathode plume morphology was presented and discussed as well as aspects related to changes in discharge current power density spectra and histograms induced by the anode position with respect to cathode exit plane.

Visual observations and discharge properties measurements were underpinned by Langmuir probe measurements in the cathode plume in order to better understand the influence of anode position on cathode discharge. The tests took place with the cathode operating at 4 A and $0.6\,\mathrm{mg\,s^{-1}}$ of xenon. Plasma properties discontinuities were reported as the cathode-anode gap approached and surpassed the value of 45 mm. Spot mode operation prevailed at low cathode-anode gap values, with higher plasma densities and lower electron temperatures, while for higher cathode-anode gap values plume mode was triggered, characterized by higher electron temperatures and lower plasma densities.

This work supports the idea that the anode position with respect to cathode exit plane is a delicate parameter to consider when characterizing cathodes in diode configuration. A randomly chosen cathode-anode gap value can induce different findings, making impossible any attempt in comparing results with similar cathodes, while the worst output remains the underestimation of the spot mode operating range. Moreover, it is worth underlying that the aforementioned results are for a flat disk emitter cathode, although they are in good agreement with similar results reported for a hollow emitter cathode [16].

Acknowledgments

This work was supported by the CNES Direction des Lanceurs Research and Technology Program. George-Cristian Potrivitu benefits from a CNRS short-term contract. Romain Joussot benefits from a CNES post-doctoral fellowship.

References

[1] S. Mazouffre, Plasma Sources Science and Technology 25 (2016) 033002. doi:10.1088/0963-0252/25/3/033002.

[2] V. Kim, K. N. Kozubsky, V. M. Murashko, A. V. Semenkin, in: 30th International Electric Propulsion Conference, Florence, Italy, September 17-20, 2007, IEPC-2007-142, pp. 1–24.

[3] D. M. Goebel, I. Katz, Fundamentals of Electric Propulsion: Ion and Hall Thrusters, JPL Space Science and Technology Series, Wiley, 2008.

[4] C. Drobny, F. Nurmberger, M. Tajmar, in: 6th Space Propulsion 2016, Rome, Italy, 02-06 May, 2016, SP2016-3124751.

[5] D. M. Goebel, R. M. Watkins, K. K. Jameson, Journal of Propulsion and Power 23 (2007) 552–558. doi:10.2514/1.25475.

[6] J. M. Lafferty, Journal of Applied Physics 22 (1951) 299–309. doi:10.1063/1.1699946.

[7] M. L. Plasek, C. J. Wordingham, S. Roja Mata, E. Choueiri, J. E. Polk, in: 50th AIAA/ASME/SAE/ASEE Joint Propulsion Conference, Cleveland (OH), U.S.A., July 28-30, 2014, AIAA 2014-3825, pp. 1–14. doi:10.2514/6.2014-3825.

[8] J. E. Polk, D. M. Goebel, P. Guerrero, in: 34th International Electric Propulsion Conference, Hyogo-Kobe, Japan, July 410, 2015, IEPC-2015-44/ISTS-2015-b-44, pp. 1–12.

[9] D. Pedrini, R. Albertoni, F. Paganucci, M. Andrenucci, Journal of Propulsion and Power 32 (2016) 1557–61. doi:10.2514/1.B35828.

[10] S. D. Grishin, L. V. Leskov, Electric Rocket Thrusters of Space Apparatus, Mashinostroenie, Moscow (in Russian), 1989.

[11] R. Joussot, L. Grimaud, S. Mazouffre, Vacuum 146 (2017) 52–62. doi:10.1016/j.vacuum.2017.09.021.

[12] L. Albarède, Etudes expérimentales d'un propulseur à effet Hall - Comportement stationnaire et dynamique du flux d'électrons, Ph.D. thesis, University of Orléans, France, 2004.

[13] Z. Ning, D. Yu, H. Li, G. Yan, Plasma Science and Technology 11 (2009) 194–199. doi:10.1088/1009-0630/11/2/12.

[14] L. Grimaud, A. Pétin, J. Vaudolon, S. Mazouffre, Review of Scientific Instruments 87 (2016) 043506. doi:10.1063/1.4945563.

[15] R. L. Washeleski, L. B. King, in: 45th AIAA/ASME/SAE/ASEE Joint Propulsion Conference & Exhibit, Denver (CO), U.S.A., 2-5 August, 2009, AIAA 2009-5199, pp. 1–21. doi:10.2514/6.2009-5199.

[16] G. A. Csiky, Measurements of some properties of a discharge from a hollow cathode, NASA Technical Note D-4966, 1969.

[17] T. M. Jack, S. W. Patterson, D. G. Fearn, in: 36th AIAA/ASME/SAE/ASEE Joint Propulsion Conference & Exhibit, Huntsville (AL), U.S.A., 16-19 July, 2000, AIAA 2000-3533.

[18] D. Lev, L. Appel, in: 6th Space Propulsion 2016, Rome, Italy, 02-06 May, 2016, SP2016-3125366.

[19] H. R. Kaufman, Technology of Electron-Bombardment Ion Thrusters, volume 36 of *Advances in Electronics and Electron Physics*, Academic Press, New-York, 1974, pp. 265–373.

[20] M. J. Mandell, I. Katz, in: 30th Joint Propulsion Conference and Exhibit, Indianapolis (IN), U.S.A., 27-29 June, 1994, AIAA 94-3134, pp. 1–6. doi:10.2514/6.1994-3134.

[21] M. Touzeau, M. Prioul, S. Roche, N. Gascon, C. Pérot, F. Darnon, S. Béchu, C. Philippe-Kadlec, L. Magne, P. Lasgorceix, D. Pagnon, A. Bouchoule, M. Dudeck, Plasma Physics and Controlled Fusion 42 (2000) B323. doi:10.1088/0741-3335/42/12B/324.

[22] A. I. Morozov, Plasma Physics Reports 29 (2003) 235–50. doi:10.1134/1.1561119.

[23] L. Albarède, V. Lago, P. Lasgorceix, M. Dudeck, A. I. Bugrova, K. Malik, in: 28th International Electric Propulsion Conference, Toulouse, France, March 17-21, 2003, IEPC-2003-333, pp. 1–18.

[24] G. Sary, R. Joussot, L. Grimaud, L. Garrigues, S. Mazouffre, B. Laurent, C. Boniface, S. Oriol, F. Masson, in: 35th International Electric Propulsion Conference, Atlanta (GA), U.S.A., October 8-12, 2017, IEPC-2017-486.

[25] M. Domonkos, A. Gallimore, G Williams Jr, M. Patterson, in: 35th Joint Propulsion Conference and Exhibit, Los Angeles (CA), U.S.A., 20-24 June, 1999, AIAA 99-2575, pp. 1–25. doi:10.2514/6.1999-2575.

[26] D. E. Siegfried, P. J. Wilbur, in: 13th International Electric Propulsion Conference, San Diego (CA), U.S.A., April 25-27, 1978, AIAA 1978-705, pp. 1–11. doi:10.2514/6.1978-705.

[27] L. Rehn, H. R. Kaufman, in: 13th International Electric Propulsion Conference, San Diego (CA), U.S.A., April 25-27, 1978, AIAA 1978-707, pp. 1–8. doi:10.2514/6.1978-707.

[28] H. J. Han, Physical processes in hollow cathode discharge, Master's thesis, Naval Postgraduate School, Moterey, CA, U.S.A., 1989.

[29] S. Sakai, T. Katayama, J. Aoyagi, H. Takegahara, in: 30th International Electric Propulsion Conference, Florence, Italy, September 1720, 2007, IEPC-2007-215, pp. 1–7.

[30] D. M. Goebel, K. K. Jameson, I. Katz, I. G. Mikellides, Physics of Plasmas 14 (2007) 103508. doi:10.1063/1.2784460.

[31] K. Nishiyama, Y. Shimizu, I. Funaki, H. Kuninaka, K. Toki, Journal of Propulsion and Power 23 (2007) 513–521. doi:10.2514/1.19473.

[32] J. D. Sommerville, L. B. King, Journal of Propulsion and Power 27 (2011) 744–753. doi:10.2514/1.50123.

[33] K. Xu, M. L. R. Walker, Journal of Propulsion and Power 30 (2014). doi:10.2514/1.B34980.

[34] D. M. Goebel, K. K. Jameson, R. M. Watkins, I. Katz, I. G. Mikellides, Journal of Applied Physics 98 (2005) 113302. doi:10.1063/1.2135417.

[35] V. Vekselman, Y. E. Krasik, S. Gleizer, V. T. Gurovich, A. Warshavsky, L. Rabinovich, Journal of Propulsion and Power 29 (2013) 475–86. doi:10.2514/1.B34628.

[36] R. Albertoni, P. Rosseti, F. P. M. Andrenucci, in: 3rd Space Propulsion 2012, Bordeaux, France, May, 2012, SP-2012-2349890.

[37] J. Heberlein, J. Mentel, E. Pfender, Journal of Physics D: Applied Physics 43 (2010) 023001. doi:10.1088/0022-3727/43/2/023001.

[38] D. Courtney, Development and Characterization of a Diverging Cusped Fied Thruster and a Lanthanum Hexaboride Hollow Cathode, Master's thesis, MIT, U.S.A., 2008.

[39] I. G. Mikellides, I. Katz, D. M. Goebel, K. K. Jameson, Journal of Applied Physics 101 (2007) 063301. doi:10.1063/1.2710763.

[40] B. A. Jorns, I. G. Mikellides, D. M. Goebel, Physical Review E 90 (2014) 063106. doi:10.1103/PhysRevE.90.063106.

[41] B. A. Jorns, C. Dodson, D. M. Goebel, R. Wirz, Physical Review E 96 (2017) 023208. doi:10.1103/PhysRevE.96.023208.
[42] M. J. Druyvesteyn, Zeitschrift für Physik 64 (1930).
[43] V. A. Godyak, R. B. Piejak, B. M. Alexandrovich, Plasma Sources Science and Technology 1 (1992).
[44] V. A. Godyak, in: 66th Gaseous Electronics Conference 2013, Princeton (NJ), U.S.A., 28-29 September,2013.
[45] D. A. Herman, A. D. Gallimore, in: 41st AIAA/ASME/SAE/ASEE Joint Propulsion Conference & Exhibit, Tucson (AZ), U.S.A., 2005, AIAA 2005-4252.
[46] T. K. Popov, M. Dimitrova, P. Ivanova, E. Hasan, J. Horáček, R. Dejarac, J. Stöckel, V. Weinzettl, J. Kovačič, Contributions to Plasma Physics 54 (2014). doi:10.1002/ctpp.201410076.